Unravelling the complex causality behind Fe–N–C degradation in fuel cells

Geunsu Bae, Minho Kim, Man Ho Han, Junsic Cho, Dong Hyun Kim, Moulay-Tahar Sougrati, Jinjong Kim, Kug-Seung Lee, Sang Hoon Joo, William Goddard, et al.

Unraveling the complex causality behind the Fe-N-C degradation in fuel cell

Geunsu Bae,[1,†] Minho M. Kim,[2,†] Song Jin,[3,4,†] Junsic Cho,[1] Dong Hyun Kim,[1] Man Ho Han,[5] Hyung-Suk Oh,[5,6] Moulay-Tahar Sougrati,[7] Kug-Seung Lee,[8] Sang Hoon Joo,[9] William A. Goddard III,[10] Hyungjun Kim,[2,] Min Ho Seo,[11,*] Frédéric Jaouen,[7,*] and Chang Hyuck Choi[1,12,*]*

[1]Department of Chemistry, Pohang University of Science and Technology (POSTECH), Pohang 37673, Republic of Korea.

[2]Department of Chemistry, Korea Advanced Institute of Science and Technology (KAIST), Daejeon 34141, Republic of Korea.

[3]School of Materials Science and Engineering, Gwangju Institute of Science and Technology (GIST), Gwangju 61005, Republic of Korea.

[4]Department of Hydrogen Energy Materials, Surface Technology Division, Korea Institute of Materials Science (KIMS), Changwon 51508, Republic of Korea.

[5]Clean Energy Research Center, Korea Institute of Science and Technology (KIST), Seoul 02792, Republic of Korea.

[6]KIST-SKKU Carbon-Neutral Research Center, Sungkyunkwan University (SKKU), Suwon 16419, Republic of Korea.

[7]ICGM, Univ. Montpellier, CNRS, ENSCM, 34293 Montpellier, France.

[8]Beamline Department, Pohang Accelerator Laboratory, Pohang University of Science and Technology (POSTECH), Pohang 37673, Republic of Korea.

[9]Department of Chemistry, Seoul National University, Seoul 08826, Republic of Korea.

[10]Materials and Process Simulation Center, California Institute of Technology, Pasadena, CA 91125, USA.

[11]Department of Nanotechnology and Engineering, Pukyong National University, Busan 48547,

Republic of Korea.

[12]Institute for Convergence Research and Education in Advanced Technology (I–CREATE), Yonsei University, Seoul 03722, Republic of Korea.

†These authors contributed equally to this work.

*Corresponding authors: linus16@kaist.ac.kr (H.K.), foifrit@pknu.ac.kr (M.H.S), frederic.jaouen@umontpellier.fr (F.J.), and chchoi@postech.ac.kr (C.H.C.)

ABSTRACT

Beyond great advances in initial activity, Fe-N-C catalysts face the next challenge of stability issue in acidic medium that must be overcome to replace Pt in fuel cell cathode. However, the complex phenomena in fuel cells and consequential difficulty in understanding deactivation mechanisms of Fe-N-C cathodes impede solutions for prolonged stability. Here, we show time-resolved changes in active site density (SD) and turnover frequency (TOF) of Fe-N-C along with concurrent decrease in oxygen reduction reaction (ORR) current in temperature/gas controllable gas-diffusion electrode (GDE) flow cell. *In operando* diagnosis of Fe leaching identifies a strong dependence of SD changes on operating parameters, and draws a lifetime-dependent stability diagram that reveals a shift in prime degradation mechanism during operation. A proof-of-concept strategy with site-isolated Pt ions as a non-catalytic stabilizer, supported by theoretical calculation, demonstrates enhanced fuel cell stability with reduced Fe dissolution, offering new design principle for durable Fe-N-C catalysts.

INTRODUCTION

On the way to the hydrogen economy, proton-exchange membrane fuel cell (PEMFC) technologies offer a promising solution for generating clean electricity with reduced pollutants and greenhouse gas emissions. Although PEMFCs have now been successfully commercialized for automobile applications with highly active and durable Pt-group metal (PGM) catalysts,[1] their cost competitiveness and sustainability issues require the replacement of PGM-based with PGM-free catalysts.[2] Especially, efforts have primarily focused on the cathode, where the sluggish oxygen reduction reaction (ORR) occurs. Among a few candidates in acidic environments, Fe-N-C catalysts comprising isolated Fe ions coordinated with nitrogen functionalities (*i.e.*, Fe-N_4) are most appealing owing to their promising initial performance.[3-5] However, their stability in PEMFCs is poor and typically shows over 40–50% of performance loss within the first tens of hours of operation at 0.5–0.6 V.[6-8] Hitherto, several degradation paths of Fe-N-C catalysts in an acidic medium have been proposed such as Fe demetallation or agglomeration,[9-11] carbon corrosion,[9,12] and surface modifications induced either by protonation of nitrogen functionalities or by reactive oxygen species (ROS).[13,14]

Although all the above mechanisms may operate to varying degrees depending on the PEMFC conditions, the primary degradation path exacerbating the prolonged PEMFC operation remains unknown. Although the degradation paths have been widely investigated on an ideal thin-film electrode in a rotating disk electrode (RDE) setup, it is worth noting that Fe-N-C cathodes in PEMFCs experience a more complex reaction venue of the triple-phase boundary, where ORR occurs at higher current density, temperature, and oxygen activity, compared to that of conventional RDE experiments. These differences may result in different nature or relative importance of degradation mechanisms, ultimately leading to considerable uncertainty in unraveling the fundamental origin of Fe-N-C deactivation in PEMFCs, as highlighted in Ehelebe's recent review.[15]

To address this issue, many efforts have been made to unveil the main degradation mechanism of Fe-N-C catalysts in PEMFC devices in recent years. For instance, Dodelet group observed serious demetallation of active Fe-N_4 moieties during the PEMFC operations using neutron activation and *post-mortem* ^{57}Fe Mössbauer spectroscopy.[7] Using similar analytical methods, Jaouen group identified a specific type of Fe-N_4 site that quickly transforms into less active (or inactive) Fe_2O_3 nanoclusters.[16] More recently, Elbaz group precisely quantified the change in number of Fe-N_4 sites *in situ* through a Fourier-transform alternating current voltammetry in PEMFCs.[17] All these cornerstone works, in which the amount of remaining active Fe moieties (and their chemical nature for the ^{57}Fe Mössbauer spectroscopy studies) were intermittently measured after a certain duration of PEMFC operations,

corroborated each other indicating the loss of active Fe as the main cause of activity decay of Fe-N-C cathodes.

However, it is worth mentioning that the PEMFC performance loss observed with Fe-N-C cathodes is rather intense during the early stages of its operation, particularly during the first few hours.[7] Although the previous diagnostic methods successfully revealed the degradation of Fe-N-C catalysts at the macroscopic level after tens of hours of PEMFC operation, they unfortunately provide intermittent information primarily because of the low temporal resolution of such end-of-test characterization approaches (Supplementary Note 1 and Supplementary Table 1). Although mathematical models have been recently developed to overcome such experimental limitations, there remains a controversy in accounting for the possible degradation pathways of Fe-N-C.[6,8] Hence, its degradation under realistic PEMFC conditions, particularly at the beginning of PEMFC operation, has not yet been clearly understood or practically surmounted. At the initial stage of PEMFC operation, multiple phenomena and significant physicochemical changes in Fe-N-C catalyst layer are expected at different rates and timescales. Therefore, it is pivotal to investigate the activity loss and deconvolute it into time-resolved modification in active site density (SD) and turnover frequency (TOF). Subsequently, such methodology would be applicable to study in detail the improved stability of Fe-N-C that can be obtained with rational approaches, accelerating the development of highly stable PGM-free cathodes.[18,19]

Herein, we unveil a time- and potential-resolved mechanistic picture behind the rapid performance loss of Fe-N-C catalysts at the early stage of their operation. Resolving this long-standing question is achieved by *in operando* monitoring of Fe dissolution from active Fe-N_4 sites using an *online* inductively coupled plasma-mass spectrometry (ICP-MS) connected to a gas-diffusion electrode (GDE)-type electrochemical flow cell (EFC). This advanced analytical platform can better mimic PEMFC environments than a conventional RDE setup. The real-time diagnosis of SD and TOF modifications under various operating conditions identifies temperature and potential as the most critical parameters triggering Fe dissolution, whereas the ultimate fate of Fe ions released by Fe-N_4 sites is strongly affected by the nature of the gas atmosphere. To mitigate the initial rapid deactivation of Fe-N-C catalyst in PEMFC, dominated by the loss of Fe-N_4 sites, we suggest that the strengthened ligation of the central Fe ion to N moieties, covalently linked to the supporting carbon network, could be a promising approach. Confirmed by density functional theory (DFT) calculation, this intuition is also experimentally corroborated with one case study catalyst that incorporates non-catalytic Pt ions as a stabilizer of the Fe-N bond and shows prolonged PEMFC operation compared to the unmodified Fe-N-C.

RESULTS and DISCUSSION

Effects of temperature on Fe dissolution of Fe-N-C

The Fe-N-C catalyst (labeled '$Fe_{0.5}NC$') was synthesized by pyrolysis of powdery precursor mixture, homogenized by ball-milling of Fe^{II} acetate, 1,10-phenanthroline (phen), and Zn^{II} zeolitic imidazolate framework (ZIF-8). As well-identified in our previous studies,[20,21] $Fe_{0.5}NC$ is solely composed of atomically dispersed Fe-N_4 moieties, the main active sites of Fe-N-C catalysts,[4,5] without noticeable amounts of bulk Fe clusters or particles. Detailed physicochemical characterizations of $Fe_{0.5}NC$ and their discussion have been provided in Supplementary Note 2 (Supplementary Fig. 1 and Supplementary Table 2). For the real-time diagnosis of SD and TOF modifications during electrochemical operations, we introduced an *online* ICP-MS combined with a GDE-based EFC (*online* GDE/EFC/ICP-MS), offering a great platform that simulates more realistic PEMFC environments than an RDE setup with controllable temperature, potential, and gas atmosphere (Fig. 1a). A detailed description of the *online* GDE/EFC/ICP-MS system has been provided in Supplementary Note 3 (Supplementary Figs. 2–5).

We first studied the effect of temperature on the Fe dissolution of $Fe_{0.5}NC$ (Fig. 1b). The Fe dissolution was analyzed with three cyclic voltammograms (CVs) in a potential range of 1.0–0.0 V *vs.* reversible hydrogen electrode (RHE) with 5 mL min^{-1} Ar flow to prevent introduction of O_2 in the system.[12,14,16] The electrolyte was de-aerated 0.1 M $HClO_4$, which continuously flowed into the EFC at 200 μL min^{-1} before introduction into ICP-MS.

At 298 K, no significant Fe dissolution was detected, suggesting the high stability of Fe-N_4 sites at ambient temperature. This conclusion aligns with our previous findings using EFC/ICP-MS with an RDE, which reported the unexpectedly high stability of Fe-N_4 moieties in acidic environments at room temperature and attributed the measured Fe dissolution to bulk Fe particles present in another ZIF-8 derived Fe-N-C catalysts with approximately twice as much Fe content.[9,10] However, we observed non-negligible dissolution of active Fe-N_4 sites at 313 K, and the dissolution rate increased with increasing temperature. Quantitatively, the cumulative amount of dissolved Fe ions was close to zero at 298 K, but it increased to 192, 842, and 993 $\mu g_{Fe}\ g_{catal}^{-1}$ at 313, 333, and 353 K, respectively. These values were greatly correlated with ORR activity loss (Fig. 1c and Supplementary Figs. 6 and 7). No significant morphological changes were observed in their transmission electron microscopy (TEM) images (Supplementary Fig. 8) after the CVs (Supplementary Fig. 9). These results pinpoint that the Fe demetallation of $Fe_{0.5}NC$ is primarily attributed to a loss of active Fe-N_4 moieties, not an artifact from imperceptible bulk Fe species or unexpected Fe impurities in the *online* GDE/EFC/ICP-MS system. This conclusion is also in line with our previous report that identified non-negligible ORR activity loss of Fe-N-C catalyst after load cycling between 0.6 and 0.9 V_{RHE} at 323 and 343 K.[9]

Despite the decisive role of temperature in activating Fe demetallation from $Fe_{0.5}NC$, the underlying dissolution mechanism seems unmodified with temperature (Fig. 1b). During the potential sweep starting from 1.0 V_{RHE}, Fe demetallation initiates at ~0.8 V_{RHE} and its rate reaches a maximum at ~0.4 V_{RHE}, independent with temperature. No obvious Fe dissolution was observed above 0.8 V_{RHE}. Although the high operating temperature may promote carbon corrosion and consequent Fe loss when the local carbon network around Fe-N_4 site is destroyed (*i.e.*, indirect Fe dissolution),[22] the enhanced Fe dissolution with decreasing potential is opposite to the potential-dependent carbon corrosion trend, which is promoted with increasing potential.[9] In addition, the potential windows triggering Fe dissolution (<0.8 V_{RHE}) and carbon corrosion (>0.9 V_{RHE}) are not identical. The results thus rule out the indirect path as the primary origin of the Fe dissolution.

To understand the Fe dissolution mechanism in more detail, we additionally carried out the potentiodynamic GDE/ICP-MS measurements at various electrolyte pHs (*i.e.*, 0.2, 1.0, 1.5, or 2.0) under Ar flow at 353 K (Supplementary Fig. 10). While no discernible Fe dissolution was detected at pH 2.0, it became magnified with decreasing electrolyte pH. The cumulative amount of dissolved Fe ions was close to zero at pH 2.0, but it increased to 329, 759, and 1237 $\mu g_{Fe}\ g_{catal}^{-1}$ at pH 1.5, 1.0, and 0.2, respectively, indicating a critical role of electrolyte pH on the Fe dissolution rate. This finding corroborates previous reports that the Fe dissolution from Fe-N_4 moieties is accompanied by the protonation of N coordination.[23,24] In addition, since the Fe dissolution from Fe-N_4 sites is expected to be dominated upon Fe^{II} after one-electron reduction of Fe^{III} (as supported by Fig. 1b), we further investigated the $Fe^{II/III}$ redox transition of $Fe_{0.5}NC$ at various pHs (Supplementary Fig. 11). A superimposition of $Fe^{II/III}$ redox potential for an RHE potential scale (*i.e.*, ~0.82 V_{RHE}) was identified, indicating that the redox reaction involves a proton transfer in the investigated pH ranges (*i.e.*, 0.2–2.0).[25]

Effects of gas atmosphere on Fe dissolution of Fe-N-C

After taking the above mechanistic picture under chemically inert Ar conditions, we then studied the Fe dissolution under concurrent ORR electrocatalysis on $Fe_{0.5}NC$ by flowing O_2 into the GDE/EFC/ICP-MS system at 353 K (Fig. 2a). Notably, under O_2 flow, the Fe dissolution rate reduces considerably. The cumulated amount is only 294 $\mu g_{Fe}\ g_{catal}^{-1}$ after three CVs, which is approximately three times lower than that under Ar (993 $\mu g_{Fe}\ g_{catal}^{-1}$). The same conclusion was made at different temperatures (Supplementary Fig. 12). This contrasts with the Fe dissolution from Fe phthalocyanine that undergoes demetallation in the presence of O_2 at 298 K,[23] not in Ar, implying different Fe dissolution behavior between the molecular level Fe complexes and pyrolyzed Fe-N-C catalysts.

Surprisingly, despite the much larger Fe leaching detected by ICP-MS under Ar than under O_2, the ORR activity drops measured after the CVs are comparable in both cases, or even slightly larger for O_2 than Ar (Fig. 2b and Supplementary Figs. 13 and 14). Similar results can also be found during a potentiostatic hold at 0.6 V_{RHE} and 353 K (Fig. 2c), typical conditions used for evaluating long-term stability of ORR catalysts.[6-8] In both Ar and O_2 flows, Fe ion starts to dissolve immediately after applying a reductive potential of 0.6 V_{RHE} and the dissolution signal converges to the background level after operation for 1 h. However, Fe dissolution amounts were different and more significant under Ar flow (1,285 $\mu g_{Fe}\ g_{catal}^{-1}$ for 1 h operation) than that under O_2 (325 $\mu g_{Fe}\ g_{catal}^{-1}$), despite considerable ORR current loss under the O_2 flow (~60% decay during 2 h, which will be discussed later in detail). Consistent conclusions were reached for other Fe-N-C catalysts beyond those derived from zeolitic imidazolate framework (ZIF; Supplementary Note 4 and Supplementary Figs. 15–19).

Subsequently, *post mortem* TEM and energy dispersive spectroscopy (EDS) analyses of the degraded $Fe_{0.5}$NC catalyst, collected from the GDE after 2 h potentiostatic hold at 0.6 V_{RHE}, were performed to investigate morphological changes (Supplementary Figs. 20 and 21). These microscopic and spectroscopic approaches provide a decisive clue for explaining the much lower Fe leaching, as detected by ICP-MS under O_2 than that of Ar. We found precipitation of Fe oxide nanoparticles in the GDE only after testing with O_2, explaining the lower amount of Fe ions detected by GDE/EFC/ICP-MS analysis in this case. The Fe oxides can stand in our operating (and even PEMFCs) conditions because of the slow dissolution kinetics and widened stable region in the Pourbaix diagram at increased temperature.[26,27] This result agrees well with Jaouen group's previous finding that discovered the formation of Fe oxides during 5–50 h of PEMFC operation using ^{57}Fe Mössbauer spectroscopy and X-ray computed tomography,[16] not only validates the successful reflection of our GDE/EFC/ICP-MS platform to PEMFC conditions but also highlights that such degradation path is highly intensive at an early stage of $Fe_{0.5}$NC polarization, only within 2 h in the present study.

Finally, based on the above findings from the GDE/EFC/ICP-MS studies with varying potential, electrolyte pH, and gas atmosphere, we can propose a Fe demetallation mechanism of Fe-N_4 sites: 1) the proton-coupled reduction of Fe^{III}-N_4 to Fe^{II}-N_4, 2) the dissolution of Fe^{II} cations into the acidic electrolyte, and 3) the protonation of N coordination, resulting in the formation of the N-H group, as supported by the density functional theory (DFT) energetics (*vide infra*).[24] In the next step, the dissolved ferrous cations can either precipitate into Fe oxides if the local O_2 concentration is favorable, or be removed as free cations from the electrode.

Real-time diagnosis of SD and TOF changes

Stemming from the considerable ORR current drops after the CV and potential hold studies performed with O_2 flow (Fig. 2a–c), our concern was oriented towards determining the number of Fe-N_4 sites that transform to Fe oxide nanoparticles during the ORR catalysis in GDE/EFC/ICP-MS. We anticipated that quantifying the formed Fe oxide nanoparticles would be the key to resolving the prime origin of the rapid catalytic loss of Fe-N-C in PEMFC, which is possible with deconvolution of SD and TOF contributions from the overall apparent activity loss. To achieve this purpose, we optimized acid leaching conditions for selective dissolution of Fe oxide nanoparticles from aged $Fe_{0.5}$NC/GDE without undesirable Fe-N_4 loss (see details in Supplementary Fig. 22), and after that, the amount of Fe oxide nanoparticles generated during the potential hold at 0.6 V_{RHE} was quantified after 30, 60, 90, or 120 min of operation at 353 K (Supplementary Figs. 23 and 24). As can be seen in Fig. 2c and Supplementary Fig. 25, the sum of cumulative amount of dissolved Fe measured by GDE/EFC/ICP-MS under O_2 flow and Fe oxide post-leaching is comparable to the cumulative amount of dissolved Fe measured under Ar flow. This suggests that the same number of Fe-N_4 sites were lost during 2 h at 0.6 V_{RHE} under Ar and O_2 flow conditions, indicating that the demetallation rate from Fe-N_4 site is quantitatively independent of the gas atmosphere used, although the underlying mechanism can be altered. This finding indicates that ROS-induced carbon corrosion is not a primary origin for Fe dissolution under the conditions we investigated.

With the SD value for pristine $Fe_{0.5}$NC, *i.e.*, 3–4 × 10^{19} sites g^{-1} (corresponding to ~20% surface utilization of Fe-N_4) that was previously measured with cyanide and nitrite probes,[28] we finally traced time-resolved modifications of SD and TOF values *in operando* from the apparent current drop during ORR catalysis (Fig. 2e and Supplementary Note 4). The ORR current density (*j*) decay at 0.6 V_{RHE} reaches −60% after 2 h operation at 0.6 V_{RHE} and 353 K. It can be classified into two zones: the first (<1 h) and second (>1 h) zones with current decay rates of 6.3 × 10^{-2} and 1.2 × 10^{-2} mA cm^{-2} min^{-1}, respectively (Fig. 2e and Supplementary Fig. 26). The continuous removal of dissolved Fe ions by electrolyte flow induces a faster activity decay in the GDE/EFC/ICP-MS system than that in PEMFC (see details in Supplementary Note 6 and Supplementary Figs. 27–30). The relative SD decrease was estimated by normalizing the total number of Fe-N_4 site lost to the initial SD value of unreacted $Fe_{0.5}$NC. The GDE/EFC/ICP-MS measurement estimated 41±2% SD loss during a 2 h potentiostatic hold at 0.6 V_{RHE} (Fig. 2e), and this value is comparable to that measured by nitrite-stripping on pristine and aged $Fe_{0.5}$NC/GDE (*i.e.*, 36% SD loss; Fig. 2f and Supplementary Fig. 31),[28,29] corroborating again that Fe dissolution and consequent activity loss is primarily due to the loss of active Fe-N_4 sites. It is worth mentioning that, even after ~40% loss of surface Fe-N_4 sites, the remaining ORR activity can still be assigned to Fe-N_4 sites that survived the operating conditions, not pristine or deactivated metal-free NC sites (Supplementary Fig. 32).

The relative TOF modifications were then derived from the corresponding relative changes in *j* and SD values. Plotting the relative loss of *j*, SD, and TOF values with operating time yields a lifetime-dependent stability diagram of Fe-N_4 site, which shows a rapid decrease in SD in the 1st zone, but it becomes considerably alleviated in the 2nd zone (Fig. 2e). In contrast, the TOF continuously decreases during the overall operating period. Therefore, this diagram successfully draws the fundamental origin of $Fe_{0.5}$NC deactivations as a function of the operation time, that is, rapid initial activity loss triggered by Fe leaching from Fe-N_4 sites, followed by gradual deactivation that mainly results from TOF decrements. The latter is likely induced by chemical oxidation of carbon surface by *operando* formed ROS (Supplementary Fig. 33).[14] Similar conclusions can be made from a stability diagram obtained with a potentiostatic hold at 0.4 V_{RHE}, but the initial decay for *j* and SD is faster than that obtained at 0.6 V_{RHE} owing to the enhanced Fe dissolution at decreased potential (Supplementary Fig. 34a–d). In addition, with a potentiostatic hold at 0.8 V_{RHE}, almost negligible SD loss results in a superimposition of the curves for *j* and TOF losses, leading to a continuous TOF loss throughout the operations (Supplementary Fig. 34e and f).

Improving Fe-N-C stability using non-catalytic stabilizer

The time-resolved deconvolution of the loss of *j* into SD and TOF values leads us to conclude that the key to securing Fe-N-C stability is minimizing the rapid demetallation of active Fe-N_4 sites at an early stage of PEMFC operation. Although TOF modification is non-negligible and of increasing importance at longer operating times,[14] several synthetic strategies for mitigating ROS formation, which have already been proven for commercialized PEMFC with Pt/C cathodes,[30,31] bring hope for securing the TOF of Fe-N-C catalysts as recently validated by introducing specific radical scavengers onto Fe-N-C cathodes in PEMFCs.[18,32]

Consequently, the next issue is to find a way to mitigate or prevent the demetallation of active Fe-N_4 sites. Previously, Mechler and coworkers achieved prolonged PEMFC operation with Fe-N-C cathode by introducing tiny amounts of Pt nanoparticles.[33] Similarly, Shao group also reported improved Fe-N-C stability after hybridization with Pt-Fe alloy nanoparticles and Pt single-atoms.[34] Both previous studies attributed the improved stability to Pt nanoparticles which reduced the production of undesirable H_2O_2 and consequently minimized ROS formation. However, the possible presence and effect of Pt single-atoms instead of Pt nanoparticles on the improved stability of Fe-N-C have to be considered. The presence of Pt single-atoms can be reasonably suspected in the former work from the non-zero valence oxidation state of Pt in X-ray photoelectron spectroscopy (XPS) study and was verified in the latter work by high-angle annular dark-field scanning transmission electron microscopy (HAADF-STEM).

Additionally, our DFT calculations suggest that the presence of a Pt-N_4 site adjacent to the Fe-N_4 site can mitigate the Fe dissolution by increasing the energy cost required (Fig. 3a and b, Supplementary Figs. 35–37, and Supplementary Table 3). Based on these calculations, we functionalized $Fe_{0.5}$NC with isolated Pt ions *via* conventional wet impregnation and H_2 reduction at 523 K (labeled '$Fe_{0.5}$NC-Pt'). The Pt loading on $Fe_{0.5}$NC was limited to only 0.5 wt%. X-ray diffraction (XRD) and Raman spectroscopy results show that the carbon structure did not alter significantly after Pt decoration (Supplementary Fig. 38). Meanwhile, in Pt L_3-edge Fourier-transformed extended X-ray absorption fine structure (FT-EXAFS), $Fe_{0.5}$NC-Pt shows a Pt-N backscattering signal at 1.9 Å without Pt-Pt interaction at 2.9 Å (Fig. 3c). In addition, the wavelet-transformed EXAFS (WT-EXAFS) contour map showed an intense peak at R ~1.9 Å and k ~6.8 $Å^{-1}$ for the Pt-N first shell (Fig. 3d). A less intense signal at R ~3.1 Å and k ~9.3 $Å^{-1}$, which is also visible for $Fe_{0.5}$NC (Supplementary Fig. 1e), is assigned to the Pt-(N)-C second shell. No signal was detected from a Pt-Pt first shell (R ~3.0 Å and k ~11.6 $Å^{-1}$, Fig. 3d). The Pt-N coordination number is close to 4 (Supplementary Table 4). Pt_{4f} XPS identified the II and IV oxidation states, and HAADF-STEM further visualized the atomic dispersion of Pt (Fig. 3e and f). Hence, these results indicated the presence of isolated Pt ions in $Fe_{0.5}$NC-Pt without appreciable amount of crystalline Pt species. Moreover, the introduction of Pt atoms did not alter the electronic structure of Fe and N compared to $Fe_{0.5}$NC, as shown by Fe K-edge X-ray absorption near edge structure (XANES), ^{57}Fe Mössbauer spectroscopy, and N_{1s} XPS (Supplementary Fig. 39 and Supplementary Table 2). This finding is consistent with our DFT models, as the calculated local magnetic moment and Bader partial charge of the Fe^{II} centres remain unchanged at 1.89 μ_B (indicating the S=1 state) and 1.10 e, respectively, even when the Pt-N_4 site is included in close proximity (Supplementary Fig. 35).

Despite those microscopic and spectroscopic evidence, the insufficient detection limit of the characterization techniques leaves uncertainty in the possible existence of minute amounts of Pt nanoparticles in $Fe_{0.5}$NC-Pt. Thus, we additionally investigated its electrocatalytic properties towards ORR, hydrogen peroxide reduction reaction (PRR), formic acid oxidation reaction (FAOR), and methanol oxidation reaction (MOR). It is of note that these reactions are accelerated on Pt nanoparticles with Pt ensemble sites, and not on isolated Pt ions.[35-37] The results show that the polarization curves of $Fe_{0.5}$NC-Pt are superimposed on those of $Fe_{0.5}$NC for all these reactions, and are entirely deviate from those of Pt/C (Fig. 3g, h, and Supplementary Fig. 40). Similarly, when Pt is functionalized on Fe-free NC (labeled 'NC-Pt'), its electrocatalytic features are similar to those of NC (Supplementary Fig. 41). Therefore, the electrocatalytic results for a broad set of reactions support the absence of crystalline Pt structures in $Fe_{0.5}$NC-Pt, and further infer that the isolated Pt site is inactive (or at least much less active than both Pt nanoparticles and Fe-N_4 sites) towards all the probe reactions.

After confirming the successful synthesis of $Fe_{0.5}$NC-Pt, we studied its stability using *online* GDE/EFC/ICP-MS at 0.6 V_{RHE} and 353 K under O_2 flow. Notably, despite its similar initial ORR

activity with $Fe_{0.5}NC$, the $Fe_{0.5}NC$-Pt reveals much better retention of ORR activity during a 2 h potentiostatic hold (−35% and −60% for $Fe_{0.5}NC$-Pt and $Fe_{0.5}NC$, respectively; Fig. 4a). The GDE/EFC/ICP-MS results measured under Ar flow show ~3 times less Fe leaching from $Fe_{0.5}NC$-Pt than $Fe_{0.5}NC$ (*i.e.*, 465 and 1,285 $\mu g_{Fe}\ g_{catal}^{-1}$, respectively; Fig. 4b), without discernable Pt dissolution (Supplementary Fig. 42). Unlike $Fe_{0.5}NC$ (Fig. 2d), the lifetime-dependent stability diagram of $Fe_{0.5}NC$-Pt shows a close interrelation of *j* loss with a decrease in TOF, rather than a decrease in SD (Supplementary Fig. 43). Thus, these results imply that the enhanced stability of $Fe_{0.5}NC$-Pt may result from the stabilization of Fe-N_4 sites against demetallation as a consequence of the introduction of isolated Pt sites in the carbon matrix.

We further found that the enhanced stability, concluded from the GDE/EFC/ICP-MS system, was also transferred to the PEMFC. At the beginning of operation, the $Fe_{0.5}NC$-Pt cathode showed similar PEMFC performance to that of the $Fe_{0.5}NC$ cathode. However, PEMFC with $Fe_{0.5}NC$-Pt cathode exhibited much superior stability during 50 h of operation at 0.5 V (Fig. 4c and d; the cell voltage corresponds to the cathode potential of ~0.6 V_{RHE} considering the anodic overpotential and Ohmic loss in PEMFC[38]). To identify whether the enhanced stability is attributed to a possible artifact originating from the *operando* agglomeration of isolated Pt sites into ORR-active particles, the $Fe_{0.5}NC$-Pt cathode was separated from the membrane-electrode assembly (MEA) after the test and *post-mortem* characterized. In the HAADF-STEM image, no discernible changes were observed in the atomic distribution of the Pt species after 50 h of PEMFC operation (Fig. 4e). In addition, the FT- and WT-EXAFS plots for the aged $Fe_{0.5}NC$-Pt revealed a dominant Pt-N interaction, without a perceptible signal from Pt-Pt interaction (Fig. 4f and Supplementary Fig. 44), almost identical to that for the pristine $Fe_{0.5}NC$-Pt. More evidently, the aged $Fe_{0.5}NC$-Pt recorded a PRR onset potential of 0.81 $V_{RHE,}$ which is much lower than that of Pt/C (0.92 V_{RHE}) and pristine $Fe_{0.5}NC$-Pt and $Fe_{0.5}NC$ (0.83 V_{RHE}), and similar to that of aged $Fe_{0.5}NC$ (0.81 V_{RHE}; Fig. 4g). The results therefore indicated no formation of highly-active Pt nanoclusters and particles during PEMFC operation. In addition, it can be ruled out that Pt single-atoms could lead to improved stability by acting as peroxide scavengers (Supplementary Note 7 and Supplementary Fig. 45). Therefore, the fundamental origin of the enhanced stability of PEMFC with $Fe_{0.5}NC$-Pt cathode is unveiled as isolated Pt-induced stabilization of catalytic Fe-N_4 sites against demetallation. Finally, even though a noble element Pt is used and the Pt-modified catalyst is not optimized in the present study, this proof-of-concept study validates that various synthetic approaches can be established to avoid significant Fe demetallation of active Fe-N_4 sites, a critical degradation path dominating a rapid performance drop during the initial PEMFC operation.

CONCLUSION

In this work, we quantitatively resolve the two key phenomena behind the rapid performance loss of the Fe-N-C cathode at an early stage of PEMFC operation. A time- and potential-resolved diagnosis, enabled by the *online* GDE/EFC/ICP-MS system, elucidates the strong dependence of Fe leaching from active Fe-N_4 moieties on operating variables, such as temperature and gas atmosphere. The former triggers Fe dissolution and determines its total amount, whereas the latter yields different fates of dissolved Fe ions. In addition, this *operando* study further enables differentiation of a real-time modification of SD and TOF values from the apparent ORR activity drop, a lifetime-dependent stability diagram that presents a clear shift of a prime deactivation path from SD loss to TOF decrease under realistic PEMFC operating conditions. Finally, we conclude that Fe demetallation is a crucial phenomenon responsible for the rapid performance drop observed during the first few hours of PEMFC operation. We show that prohibiting undesirable Fe demetallation and consequently enhancing PEMFC stability are synthetically available by introducing site-isolated Pt ions onto the Fe-N-C catalyst, the concept inspired by previous works and our DFT calculations. Therefore, this new understanding suggests that the development of novel synthetic routes involving non-PGM stabilizers of Fe-N_4 sites could bring hope for the future reality of Fe-N-C catalysts for commercial PEMFCs.

Methods

Catalyst synthesis. $Fe_{0.5}NC$ catalyst was prepared from Fe^{II} acetate (98%, Sigma-Aldrich), 1,10-phenanthroline (phen; ≥99%, Sigma-Aldrich), and Zn^{II} zeolitic framework (ZIF-8, Basolite Z1200, BASF). One gram of the precursor mixture containing 0.5 wt% Fe and a mass ratio of phen/ZIF-8 of 20/80 were mixed using dry ball-milling for four cycles of 30 min at 400 rpm. A ZrO_2 crucible with 100 ZrO_2 balls of 5 mm diameter was used in this procedure. The resulting precursors were pyrolyzed at 1323 K under Ar flow for 1 h. $Fe_{0.5}NC$ contained Fe content of *ca.* 1.5 wt%, as confirmed by inductively coupled plasma-optical emission spectroscopy (ICP-OES). For the synthesis of $Fe_{0.5}NC$-Pt, 0.5 wt% Pt was impregnated on $Fe_{0.5}NC$ by conventional wet impregnation and subsequent H_2 reduction. 0.1 g $Fe_{0.5}NC$ was dissolved and dispersed in 100 mL of deionized water containing 1.3 mg of $H_2PtCl_6 \cdot 6H_2O$ (≥37.5%, Pt basis, Merck), and then the solvent was evaporated at 353 K. The resultant powder sample was dried at 353 K under vacuum overnight and reduced at 523 K for 3 h under H_2 flow (5%, 200 mL min^{-1}). Commercial Pt nanoparticle (HiSPEC 3000, 20 wt% Pt) was purchased from Thermo Fisher Scientific. For the synthesis of Fe_2O_3/NC, the NC catalyst was first prepared identically to $Fe_{0.5}NC$, except for the addition of Fe^{II} acetate during the ball-milling step. Note that owing to the presence of trace amounts of Fe impurities in the commercial ZIF-8 (>100 ppm),[39] Fe-free ZIF-8 was used for the synthesis of NC, which was prepared by mixing 2-methylimidazole (2-MeIm; 99%, Sigma-Aldrich) and Zn nitrate hexahydrate (Zn salt; 98%, Sigma-Aldrich) in aqueous solution (Zn salt/2-MeIm/water molar ratio of 1/60/2228).[40] A, Fe_2O_3/NC was synthesized by a dry ball-milling of 98 mg NC and 2 mg commercial Fe_2O_3 (96%, Sigma-Aldrich) for four cycles of 30 min at 400 rpm without heat treatment. The Fe content in Fe_2O_3/NC was *ca.* 1.3 wt%, as confirmed by ICP-OES. Commercial Fe-N-C catalyst (no. PMF-0110904, Pajarito Powder) was purchased from Pajarito Powder Inc, which is synthesized *via* hard templating with fumed silica. The carbon nanotube (CNT)-supported Fe-N-C catalyst (FeNC/CNT) was synthesized using a silica-protective-layer-assisted approach.[41] 100 mg of nitric acid-treated CNTs (Carbon Nanomaterial Technology Co., Ltd) were mixed with 200 mg of Fe^{III}TMPPCl (Porphyrin Systems) in an agate mortar for 5 min. The mixture was heated in a quartz-tube furnace, starting from room temperature to 673 K, at a ramping rate of 275 K min^{-1} and kept at that temperature for 3 h under N_2 gas (99.999%) flowing at a rate of 1 L min^{-1}. Afterwards, the heat-treated CNT/Fe^{III}TMPPCl composite was mixed with 0.5 mL of TEOS in a mortar, followed by mixing with 0.5 mL of formic acid. The resulting mixture was transferred ton an alumina crucible and dried in a 333 K oven for 3 h. Subsequently, the composite was heated to 1073 K at a ramping rate of 275 K min^{-1} and maintained at that temperature for 3 h under N_2 gas flowing at a rate of 1 L min^{-1}. To etch the silica, the resulting composite was mixed with 2:1 (v/v) solution of ethanol and 10% aqueous HF, and stirred for 30 min. The mixture was then filtered and washed with ethanol multiple times. The HF

etching process was repeated following the same procedure, and the resulting sample was dried at 333 K to obtain FeNC/CNT samples.

Physicochemical characterization. X-ray diffraction (XRD) patterns were obtained using a high-resolution X-ray diffractometer (X'Pert PRO MPD, PANalytical) equipped with a Cu K_α X-ray source. The XRD patterns were measured at an accelerating voltage of 60 kV and current of 55 mA, with scan rate of 10° min^{-1} and step size of 0.02°. Raman spectra were obtained using a NRS-5000 series Raman spectrometer (JASCO) with 633 nm laser excitation. XPS measurements were performed using *K*-Alpha$^+$ (Thermo Scientific) instrument equipped with a micro-focused monochromator X-ray source. The binding energy used for the peak deconvolution of the XPS-Pt spectra (for $4f_{7/2}$) was 72.4 and 73.8 eV for Pt^{II} and Pt^{IV}, respectively, and the spin-orbit splitting for $4f_{5/2}$ and $4f_{7/2}$ peaks was 3.33 eV.[42] ICP-OES analysis was performed using Optima 4300 DV (PerkinElmer Inc.) for determining Fe contents. Fe K-edge or Pt L_3-edge X-ray absorption spectroscopy (XAS) signals were collected in the transmission mode at the Pohang Accelerator Laboratory (8C, Nano XAFS). To compensate any energy shift during data acquisition, the XAS energy scale was calibrated using each metal foil before the measurements. The XANES and EXAFS analyses were conducted using Athena and Artemis implemented in the Demeter program package. The EXAFS data in *k* space was Fourier-transformed with the Hanning window function (dk = 0.5 $Å^{-1}$) after k^3-weighting. Curve fitting of the FT-EXAFS of $Fe_{0.5}$NC-Pt was carried out in the *R*-range of 1.1–2.3 Å with phase correction by including Pt–N and Pt–Cl scattering paths. The amplitude reduction factor (S_0^2) for Pt was determined to be 0.83 from the curve fitting of the EXAFS of the Pt foil. The wavelet-transform of k^3-weighted EXAFS data was analyzed with phase correction using the HAMA Fortran code. A Morlet function was used for the mother wavelet function (η = 10, σ = 1). The ^{57}Fe Mössbauer spectrum was acquired using a ^{57}Co source in Rh. The measurement was performed by keeping both the source and absorber at 7 K. The spectrometer was operated with a triangular velocity waveform, and a NaI scintillation detector was used to detect γ-rays. TEM, EDS, and HAADF-STEM analyses were performed using TECNAI G2 F30 S-Twin (FEI), TECNAI F20 UT (FEI), and Titan 80-300 (FEI), respectively.

Electrochemical measurements. The electrochemical properties were investigated using a VMP-300 potentiostat (Bio-Logic) in a three-electrode cell equipped with a graphite rod counter electrode and saturated Ag/AgCl reference electrode (RE-1A, EC-Frontier). A 0.1 M $HClO_4$ electrolyte was prepared using ultrapure water (>18 MΩ, Sartorious) and concentrated $HClO_4$ (70%, Sigma-Aldrich). The reference electrode was calibrated against a Pt electrode in an H_2-saturated electrolyte at various temperatures to convert the potentials to the RHE scale correctly. To prevent any undesirable changes in the equilibrium potential of the reference electrode, we maintained its temperature at room temperature during experiments (Supplementary Fig. 2). The catalyst ink was prepared by dispersing 10 mg of the catalyst in an aqueous solution (868 μL deionized water, 7 μL isopropanol, and 80 μL

5 wt% Nafion solution). After ultra-sonication of the above suspension for 30 min, the working electrodes were prepared by dropping 15 μL of catalyst ink onto a glassy carbon disk (0.196 cm^2) of the RDE (01169, ALS). The catalyst loadings were set to 800 μg cm^{-2} for $Fe_{0.5}NC$ or $Fe_{0.5}NC$-Pt, and 10 μg_{Pt} cm^{-2} for Pt nanoparticles. The ORR polarization curves were recorded with a scan rate of 10 mV s^{-1} and rotation speed of 900 rpm in an O_2-saturated 0.1 M $HClO_4$ electrolyte. ORR Faradaic currents were obtained by subtracting the polarization curves measured in an Ar-saturated electrolyte. The PRR polarization curves were measured with a scan rate of 1 mV s^{-1} and a rotation speed of 900 rpm in an Ar-saturated 0.1 M $HClO_4$ electrolyte containing 1.3 mM H_2O_2. Nitrite stripping experiment was conducted on the $Fe_{0.5}NC$ catalysts collected from the $Fe_{0.5}NC$/GDE before and after a 2 h potentiostatic hold at 0.6 V_{RHE} and 353 K under Ar flow. The catalyst ink was prepared by dispersing the catalyst in an aqueous solution (267 μL deionized water, 25 μL isopropanol, and 2 μL 5 wt% Nafion solution). After ultra-sonication of the above suspension for 30 min, the working electrodes were prepared by dropping 75 μL of catalyst ink onto a glassy carbon disk (0.196 cm^2) of the RDE (01169, ALS). The catalyst loading was set to 50 μg cm^{-2}.

Online GDE/EFC/ICP-MS measurements. The GDE was fabricated by spraying catalyst ink onto a mesoporous layer (MPL) deposited on carbon paper. On a carbon paper with a 20 wt% polytetrafluoroethylene (PTFE) content (2 × 2 cm^2, TGP-H-090, Toray), highly hydrophobic carbon MPL was first fabricated by spraying an ink emulsion containing 100 mg Ketjen black EC-300J, 400 mg PTFE (60 wt%, Sigma-Aldrich), and 20 mL isopropyl alcohol (IPA, 99.5%, Sigma-Aldrich), followed by heat-treatment at 513 and 613 K under Ar atmosphere for 30 min each. The resulting MPL had a Ketjen Black EC-300J loading of 2 mg cm^{-2}. Thereafter, catalyst ink (25 mg catalyst + 10 mL isopropanol + 250 μL 5 wt% Nafion solution) was sprayed onto the MPL to reach target catalyst loadings of 400 μg cm^{-2}. The active catalyst area of the GDE was 0.096 cm^2. Fe dissolution was monitored using ICP-MS (7500ce, Agilent) coupled with a GDE-based EFC. The EFC is equipped with a U-shaped channel with a diameter of 1 mm and an opening for contact with the GDE. A graphite tube counter electrode (inner diameter = 1 mm) was placed at the inlet, and an Ag/AgCl reference electrode was connected to the outlet of EFC. A 0.1 M $HClO_4$ electrolyte, de-aerated using a degasser (AG-32-01, FLOM Corp.), was flowed into the EFC at a flow rate of 200 μL min^{-1}. The electrolyte was mixed with 0.2 M HNO_3 containing 5 ppb ^{187}Re as an internal standard using a Y-connector (mixing ratio = 1:1). Ar or O_2 gases flowed into the graphite serpentine gas channel at a rate of 5 mL min^{-1}. GDE was pre-treated with 200 fast CV cycles (200 mV s^{-1}) in the potential range of 1.0−0.0 V_{RHE} at 298 K before the electrochemical measurement. After stabilization at the desired temperature for *ca.* 10 min, Fe dissolution was analyzed under potentiodynamic or potentiostatic conditions. Fe dissolution under potentiodynamic conditions was analyzed with three slow CV cycles (5 mV s^{-1}) in the potential range of 1.0−0.0 V_{RHE} at various temperatures (298, 313, 333, and 353 K) under Ar or O_2 flow. Fe dissolution

under potentiostatic conditions was analyzed by holding 0.4, 0.6, or 0.8 V_{RHE} at 353 K under Ar or O_2 flow. ORR polarization curves were recorded with a scan rate of 5 mV s^{-1} at 298 K. A manual *iR* compensation (MIR) program was used to compensate 85% of ohmic drop during the electrochemical measurements and 15% post-corrected. The uncompensated resistance was measured using electrochemical impedance spectroscopy (EIS) at open circuit potential (OCP; Supplementary Fig. 46).

Computational Details. Spin-polarized DFT calculations were conducted by using the Vienna ab initio Simulation Package (VASP) 5.4.4.[43] The projector-augmented wave (PAW) pseudopotential and Perdew-Burke-Ernzerhof (PBE) exchange-correlation functional were applied for all calculations.[44,45] For the plane-wave basis, the kinetic energy cutoff was set as 520 eV. The first order of the Methfessel-Paxton (MP) method was used with a smearing width of 0.05 eV.[46] A (5×5×1) Γ-centered *k*-point grid was used to sample the reciprocal space. The convergence criterion was set as 1×10^{-5} eV for the electronic step, and 0.01 eV $Å^{-1}$ for the ionic relaxation step. Atomic partial charges were calculated using the Bader charge analysis.[47]

For accurate calculations of the slab geometry, an additional vacuum region was included with a dipole correction to eliminate electrostatic interactions between periodic images along the surface normal direction. The (6×6) surface unit cell of graphene served as the base structure for investigating eight different Fe-N_4 system structures, wherein the locations of the Pt-N_4 site were varied. Additionally, three additional structures were explored by varying the intersite distance between Fe-N_4 and Pt-N_4, using the base structure of an (8×8) surface unit cell of graphene (Supplementary Figs. 35 and 36). For the formation energy calculations, the reference states of H, C, N, Fe, and Pt were chosen as H_2, graphite, N_2, α-phase of Fe solid, and face-centred-cubic Pt solid, respectively.

For the calculation of energy profiles concerning the Fe dissolution reaction at electrified (or charged) interfaces, the VASPsol package employing the implicit solvation method was utilized. The Debye length was set at 0.304 nm^{-1}, and the dielectric constant was set at 78.4. In our slab model of the Fe-N_4 system, a charge of +2 was applied, resulting in an electrochemical potential of 0.36 V_{RHE}, which closely corresponds to the experimental conditions. To investigate the energetics of nonelectrochemical reactions, the system charge was then adjusted based on the charge states of reactants and products; specifically, the system charge was decreased by 2 for the removal of Fe^{II} and increased by 1 for each added proton. Three possible reaction paths were investigated; the most plausible reaction mechanism is shown in Figure 3a and b, while the others are presented in Supplementary Figure 37. The energy state of Fe^{II}(aq) was calculated by evaluating the ionization energy of Fe and the solvation-free energy of Fe^{II} using Jaguar 10.9 software[48] (B3LYP functional[49] with LANL2DZ basis set[50]) as coupled with the Poisson-Boltzmann implicit solvation model[51] (Supplementary Note 8).

PEMFC operation. MEA was prepared by a decal process *via* doctor blade coating to compare the single cell performance of $Fe_{0.5}NC$ and $Fe_{0.5}NC$-Pt as cathode catalysts with all the Pt/C-based anodes. The cathode slurries were prepared by dispersing 0.26 g catalysts ($Fe_{0.5}NC$ and $Fe_{0.5}NC$-Pt) in an aqueous solution containing 0.18 g deionized water, 0.14 g isopropanol, 0.14 g n-propanol, and 0.431 g 20 wt% Nafion solution (1000 EW, DuPont Fuel Cells). Moreover, the anode slurries were prepared by mixing 0.35 g catalysts (37.7 wt% Pt/C, TANAKA Precious metals) in an aqueous solution containing 1.98 g deionized water, 0.40 g isopropanol, and 2.30 g 5 wt% Nafion solution (1100 EW, DuPont Fuel Cells). The Nafion ionomer content in both the anode and cathode slurries was adjusted to 25 wt% of the total electrode solid amount. The slurries prepared in the N_2-filled glove box were stirred in an ultrasonic water bath for 2 h, followed by a three-roll milling process (EXAKT 50I) to effectively break up the agglomerates in the slurries. The mixture was then stirred in an ultrasonic water bath for 1 h for better dispersion. Each cathode and anode slurry was coated onto a PTFE film as a decal substrate using a doctor-blade coater. The coated electrodes were dried at 353 K in an N_2-purged vacuum oven, and the prepared cathode was hot-pressed onto a Nafion 211 membrane with an anode electrode at 100 bar and 383 K for 10 min. After cooling for 10 min *via* the cooling press, we successfully obtained MEA with an active area of 25 cm^2. The catalyst contents of the cathode and anode electrodes were controlled at approximately 4.0 and 0.25 mg cm^{-2}, respectively. The cell performance of MEA was evaluated using an EIS46 potentiostat (Bio-Logic, HCP-803). The single-cell includes the MEA, gas diffusion layers (320 μm thickness, JNTG), bipolar plates constituting serpentine channels of graphite, and current collector plates made of gold-coated copper blocks. Before evaluating the cell performance, a break-in process was conducted in the following steps: (1) H_2 and O_2 with 500 and 1,500 mL min^{-1} flow rates with the condition of 100% relative humidity (RH) at 353 K were provided for the anode and cathode, respectively. (2) A 0.1 V per step was applied for 30 s in the cycling range of 0.3–0.7 V until the performance of MEA at 0.6 V was stabilized. To evaluate the cell performance, polarization curves were obtained at ambient pressure, and the cell voltage decreased from open circuit voltage (OCV) to 0.2 V at a scan rate of 20 mV s^{-1} by linear sweep voltammetry under the same operating conditions as that of the activation process.

DATA AVAILABILTY

The data supporting the findings of this study are available within this article and its Supplementary Information files, or from the corresponding author upon reasonable request.

ASSOCIATED CONTENT

Supplementary Information

The following file is available free of charge.

Physicochemical characteristics of $Fe_{0.5}NC$ and $Fe_{0.5}NC$-Pt; description of online GDE/EFC/ICP-MS system; ORR polarization curves before and after CVs; *post-mortem* characterization data; post-leaching experiment results; model structures for DFT calculation and summary of cohesive energy values; additional electrochemical characterization data; additional GDE/EFC/ICP-MS results (PDF)

AUTHOR INFORMATION

Authors and Affiliations

Department of Chemistry, Pohang University of Science and Technology (POSTECH), Pohang 37673, Republic of Korea.

Geunsu Bae, Junsic Cho, Dong Hyun Kim, and Chang Hyuck Choi

Department of Chemistry, Korea Advanced Institute of Science and Technology (KAIST), Daejeon 34141, Republic of Korea.

Minho M. Kim and Hyungjun Kim

School of Materials Science and Engineering, Gwangju Institute of Science and Technology (GIST), Gwangju 61005, Republic of Korea.

Song Jin

Department of Hydrogen Energy Materials, Surface Technology Division, Korea Institute of Materials Science (KIMS), Changwon 51508, Republic of Korea.

Song Jin

Clean Energy Research Center, Korea Institute of Science and Technology (KIST), Seoul 02792, Republic of Korea.

Man Ho Han & Hyung-Suk Oh

KIST-SKKU Carbon-Neutral Research Center, Sungkyunkwan University (SKKU), Suwon 16419, Republic of Korea.

Hyung-Suk Oh

ICGM, Univ. Montpellier, CNRS, ENSCM, 34293 Montpellier, France.
Moulay-Tahar Sougrati & Frédéric Jaouen

Beamline Department, Pohang Accelerator Laboratory, Pohang University of Science and Technology (POSTECH), Pohang 37673, Republic of Korea.
Kug-Seung Lee

Department of Chemistry, Seoul National University, Seoul 08826, Republic of Korea.
Sang Hoon Joo

Materials and Process Simulation Center, California Institute of Technology, Pasadena, CA 91125, USA.
William A. Goddard III

Department of Nanotechnology and Engineering, Pukyong National University, Busan 48547, Republic of Korea.
Min Ho Seo

Institute for Convergence Research and Education in Advanced Technology (I–CREATE), Yonsei University, Seoul 03722, Republic of Korea.
Chang Hyuck Choi

Corresponding Authors

*Hyungjun Kim
−Email: linus16@kaist.ac.kr

*Min Ho Seo
−Email: foifrit@pknu.ac.kr

*Frédéric Jaouen
−Email: frederic.jaouen@umontpellier.fr

*Chang Hyuck Choi
−Email: chchoi@postech.ac.kr

Author Contributions

C.H.C., F.J., M.H.S., and H.K. conceived and supervised the project. G.B. conducted most of the experimental analyses. M.M.K. conducted DFT calculations. S.J. conducted a fuel cell experiment. J.C. and D.H.K. contributed to the part of electrochemical analyses. M.H.H. and H.-S.O. contributed to HAADF-STEM analysis. M.-T.S. contributed to ^{57}Fe Mössbauer spectroscopy measurement. K.-S.L contributed to XAS measurement. S. H. J. contributed to part of the catalyst synthesis. W. G. contributed

to DFT calculations. The manuscript was written through the contributions of all authors. †These authors contributed equally.

ETHICS DECLARATIONS

Competing Interests

The authors declare no competing financial interest.

ACKNOWLEDGMENTS

This research was supported by the National Research Foundation of Korea (NRF) grant funded by the Korea government (MSIT) (No. 2019M3D1A1079309, 2021R1A5A1030054, and 2022R1A2C2093090) and by the KIST Institutional Program. The authors acknowledge the Pohang Accelerator Laboratory (PAL) for beamline use (8C, PLS-II).

References

1 Yoshida, T. & Kojima, K. Toyota MIRAI fuel cell vehicle and progress toward a future hydrogen society. *Electrochem. Soc. Interface* **24**, 45-49 (2015).

2 Thompson, S. T. & Papageorgopoulos, D. Platinum group metal-free catalysts boost cost competitiveness of fuel cell vehicles. *Nat. Catal.* **2**, 558-561 (2019).

3 Proietti, E. *et al.* Iron-based cathode catalyst with enhanced power density in polymer electrolyte membrane fuel cells. *Nat. Commun.* **2**, 416 (2011).

4 Chung, H. T. *et al.* Direct atomic-level insight into the active sites of a high-performance PGM-free ORR catalyst. *Science* **357**, 479-484 (2017).

5 Lefèvre, M., Proietti, E., Jaouen, F. & Dodelet, J.-P. Iron-based catalysts with improved oxygen reduction activity in polymer electrolyte fuel cells. *Science* **324**, 71-74 (2009).

6 Yin, X. & Zelenay, P. (Invited) Kinetic models for the degradation mechanisms of PGM-free ORR catalysts. *ECS Trans.* **85**, 1239-1250 (2018).

7 Chenitz, R. *et al.* A specific demetalation of Fe–N_4 catalytic sites in the micropores of NC_Ar + NH_3 is at the origin of the initial activity loss of the highly active Fe/N/C catalyst used for the reduction of oxygen in PEM fuel cells. *Energy Environ. Sci.* **11**, 365-382 (2018).

8 Zhang, G. *et al.* Non-PGM electrocatalysts for PEM fuel cells: effect of fluorination on the activity and stability of a highly active NC_Ar + NH_3 catalyst. *Energy Environ. Sci.* **12**, 3015-3037 (2019).

9 Choi, C. H. *et al.* Stability of Fe-N-C catalysts in acidic medium studied by operando spectroscopy. *Angew. Chem. Int. Ed.* **54**, 12753-12757 (2015).

10 Choi, C. H. *et al.* Minimizing operando demetallation of Fe-N-C electrocatalysts in acidic medium. *ACS Catal.* **6**, 3136-3146 (2016).

11 Kumar, K. *et al.* Fe–N–C electrocatalysts' durability: effects of single atoms' mobility and clustering. *ACS Catal.* **11**, 484-494 (2021).

12 Kumar, K. *et al.* On the influence of oxygen on the degradation of Fe-N-C catalysts. *Angew. Chem. Int. Ed.* **59**, 3235-3243 (2020).

13 Herranz, J. *et al.* Unveiling N-protonation and anion-binding effects on Fe/N/C Catalysts for O_2 reduction in proton-exchange-membrane fuel cells. *J. Phys. Chem. C* **115**, 16087-16097 (2011).

14 Choi, C. H. *et al.* The Achilles' heel of iron-based catalysts during oxygen reduction in an acidic medium. *Energy Environ. Sci.* **11**, 3176-3182 (2018).

15 Ehelebe, K., Escalera-López, D. & Cherevko, S. Limitations of aqueous model systems in the stability assessment of electrocatalysts for oxygen reactions in fuel cell and electrolyzers. *Curr. Opin. Electrochem.* **29**, 100832 (2021).

16 Li, J. *et al.* Identification of durable and non-durable FeN_x sites in Fe–N–C materials for proton exchange membrane fuel cells. *Nat. Catal.* **4**, 10-19 (2021).

17 Snitkoff-Sol, R. Z. *et al.* Quantifying the electrochemical active site density of precious metal-free catalysts in situ in fuel cells. *Nat. Catal.* **5**, 163-170 (2022).

18 Xie, H. *et al.* Ta–TiO_x nanoparticles as radical scavengers to improve the durability of Fe–N–C oxygen reduction catalysts. *Nat. Energy* **7**, 281-289 (2022).

19 Liu, S. *et al.* Atomically dispersed iron sites with a nitrogen–carbon coating as highly active and durable oxygen reduction catalysts for fuel cells. *Nat. Energy* **7**, 652-663 (2022).

20 Zitolo, A. *et al.* Identification of catalytic sites for oxygen reduction in iron- and nitrogen-doped graphene materials. *Nat. Mater.* **14**, 937-942 (2015).

21 Kim, D. H. *et al.* Selective electrochemical reduction of nitric oxide to hydroxylamine by atomically dispersed iron catalyst. *Nat. Commun.* **12**, 1856 (2021).

22 Goellner, V. *et al.* Degradation of Fe/N/C catalysts upon high polarization in acid medium. *Phys. Chem. Chem. Phys.* **16**, 18454-18462 (2014).

23 Chen, Z. *et al.* Operando characterization of iron phthalocyanine deactivation during oxygen reduction reaction using electrochemical tip-enhanced Raman spectroscopy. *J. Am. Chem. Soc.* **141**, 15684-15692 (2019).

24 Holby, E. F., Wang, G. & Zelenay, P. Acid stability and demetalation of PGM-free ORR electrocatalyst structures from density functional theory: a model for “single-atom catalyst” dissolution. *ACS Catal.* **10**, 14527-14539 (2020).

25 Jia, Q. *et al.* Spectroscopic insights into the nature of active sites in iron–nitrogen–carbon electrocatalysts for oxygen reduction in acid. *Nano Energy* **29**, 65-82 (2016).

26 Beverskog, B. & Puigdomenech, I. Revised pourbaix diagrams for iron at 25–300 °C. *Corros. Sci.* **38**, 2121-2135 (1996).

27 K. M. Parida, N. N. D. Reductive dissolution of hematite in hydrochloric acid medium by some inorganic and organic reductants: a comparative study. *Indian J. Eng. Mater. Sci.* **3**, 243 (1996).

28 Bae, G. *et al.* Quantification of active site density and turnover frequency: from single-atom metal to nanoparticle electrocatalysts. *JACS Au* **1**, 586-597 (2021).

29 Malko, D., Kucernak, A. & Lopes, T. *In situ* electrochemical quantification of active sites in Fe–N/C non-precious metal catalysts. *Nat. Commun.* **7**, 13285 (2016).

30 Lei, M. *et al.* CeO_2 nanocubes-graphene oxide as durable and highly active catalyst support for proton exchange membrane fuel cell. *Sci. Rep.* **4**, 7415 (2014).

31 Wang, L., Advani, S. G. & Prasad, A. K. Degradation reduction of polymer electrolyte membranes using CeO_2 as a free-radical scavenger in catalyst layer. *Electrochim. Acta* **109**, 775-780 (2013).

32 Bae, G., Chung, M. W., Ji, S. G., Jaouen, F. & Choi, C. H. pH effect on the H_2O_2-induced deactivation of Fe-N-C catalysts. *ACS Catal.* **10**, 8485-8495 (2020).

33 Mechler, A. K. *et al.* Stabilization of iron-based fuel cell catalysts by non-catalytic platinum. *J. Electrochem. Soc.* **165**, F1084-F1091 (2018).

34 Xiao, F. *et al.* Atomically dispersed Pt and Fe sites and Pt–Fe nanoparticles for durable proton exchange membrane fuel cells. *Nat. Catal.* **5**, 503-512 (2022).

35 Choi, C. H. *et al.* Hydrogen peroxide synthesis via enhanced two-electron oxygen reduction pathway on carbon-coated Pt surface. *J. Phys. Chem. C* **118**, 30063-30070 (2014).

36 Ferre-Vilaplana, A., Perales-Rondón, J. V., Buso-Rogero, C., Feliu, J. M. & Herrero, E. Formic acid oxidation on platinum electrodes: a detailed mechanism supported by experiments and calculations on well-defined surfaces. *J. Mater. Chem. A* **5**, 21773-21784 (2017).

37 Chung, D. Y., Lee, K.-J. & Sung, Y.-E. Methanol electro-oxidation on the Pt surface: revisiting the cyclic voltammetry interpretation. *J. Phys. Chem. C* **120**, 9028-9035 (2016).

38 Neyerlin, K. C., Gu, W., Jorne, J. & Gasteiger, H. A. Study of the exchange current density for the hydrogen oxidation and evolution reactions. *J. Electrochem. Soc.* **154**, B631 (2007).

39 Zhang, G., Chenitz, R., Lefèvre, M., Sun, S. & Dodelet, J.-P. Is iron involved in the lack of stability of Fe/N/C electrocatalysts used to reduce oxygen at the cathode of PEM fuel cells? *Nano Energy* **29**, 111-125 (2016).

40 Kida, K., Okita, M., Fujita, K., Tanaka, S. & Miyake, Y. Formation of high crystalline ZIF-8 in an aqueous solution. *CrystEngComm* **15**, 1794-1801 (2013).

41 Sa, Y. J. *et al.* A general approach to preferential formation of active Fe–N_x sites in Fe–N/C electrocatalysts for efficient oxygen reduction reaction. *J. Am. Chem. Soc.* **138**, 15046-15056 (2016).

42 Badam, R., Vedarajan, R., Okaya, K., Matsutani, K. & Matsumi, N. Sacrificial reducing agent free photo-generation of platinum nano particle over carbon/TiO_2 for highly efficient oxygen reduction reaction. *Sci. Rep.* **6**, 37006 (2016).

43 Kresse, G. & Furthmüller, J. Efficiency of ab-initio total energy calculations for metals and semiconductors using a plane-wave basis set. *Comput. Mater. Sci.* **6**, 15-50 (1996).

44 Kresse, G. & Furthmüller, J. Efficient iterative schemes for ab initio total-energy calculations using a plane-wave basis set. *Phys. Rev. B* **54**, 11169-11186 (1996).

45 Perdew, J. P., Burke, K. & Ernzerhof, M. Generalized gradient approximation made simple. *Phys. Rev. Lett.* **77**, 3865-3868 (1996).

46 Methfessel, M. & Paxton, A. T. High-precision sampling for Brillouin-zone integration in metals. *Phys. Rev. B* **40**, 3616-3621 (1989).

47 Henkelman, G., Arnaldsson, A. & Jónsson, H. A fast and robust algorithm for Bader decomposition of charge density. *Comput. Mater. Sci.* **36**, 354-360 (2006).

48 Becke, A. D. Density-functional thermochemistry. III. The role of exact exchange. *J. Chem. Phys.* **98**, 5648-5652 (1993).
49 Hay, P. J. & Wadt, W. R. Ab initio effective core potentials for molecular calculations. Potentials for the transition metal atoms Sc to Hg. *J. Chem. Phys.* **82**, 270-283 (1985).
50 Bochevarov, A. D. *et al.* Jaguar: A high-performance quantum chemistry software program with strengths in life and materials sciences. *Int. J. Quantum Chem.* **113**, 2110-2142 (2013).
51 Friedrichs, M., Zhou, R., Edinger, S. R. & Friesner, R. A. Poisson−Boltzmann analytical gradients for molecular modeling calculations. *J. Chem. Phys. B* **103**, 3057-3061 (1999).

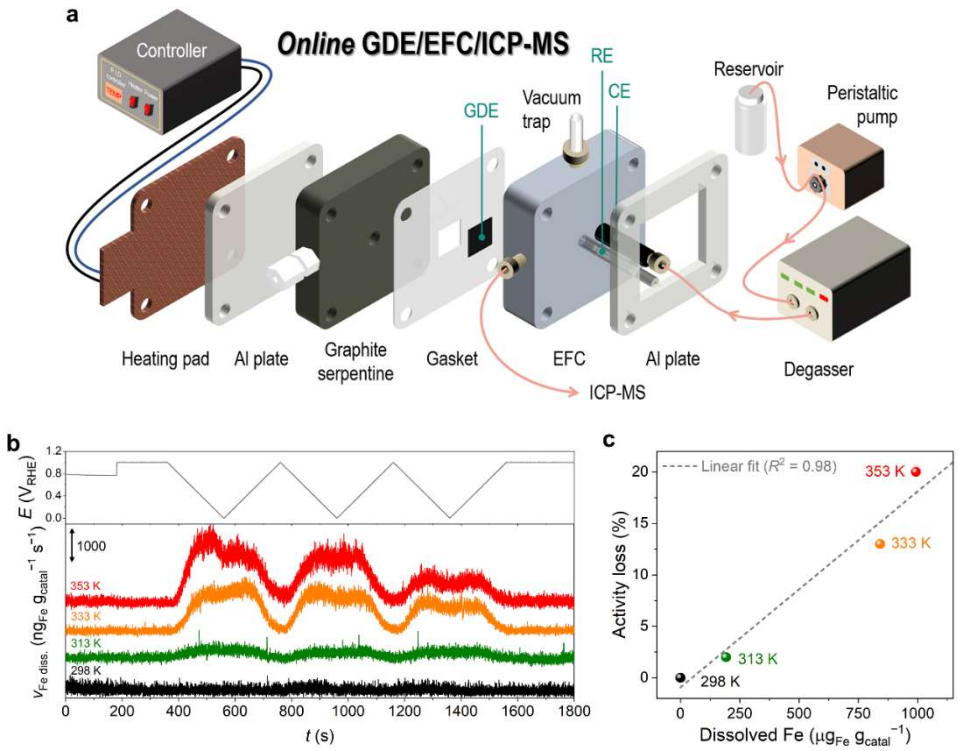

Fig. 1. Effects of temperature on Fe dissolution of $Fe_{0.5}NC$. a, Scheme of *online* GDE/EFC/ICP-MS. An electrolyte de-aerated by the degasser continuously flowed into the EFC, which was composed of the counter and reference electrodes (CE and RE, respectively) and the vacuum trap. PTFE-treated GDE, on which $Fe_{0.5}NC$ was deposited, was used as the working electrode. The electrolyte outlet was connected to ICP-MS. **b**, Real-time Fe dissolution of $Fe_{0.5}NC$/GDE obtained by *online* GDE/EFC/ICP-MS during the three CVs in a potential range of 1.0–0.0 V_{RHE} under Ar flow at various temperatures (*i.e.*, 298, 313, 333, and 353 K). The electrolyte was de-aerated 0.1 M $HClO_4$. **c**, Correlation between the cumulative amounts of dissolved Fe and the ORR activity loss obtained after the three CVs at various temperatures. The activity loss was recorded at 0.8 V_{RHE} after the CVs (Supplementary Figs. 6 and 7).

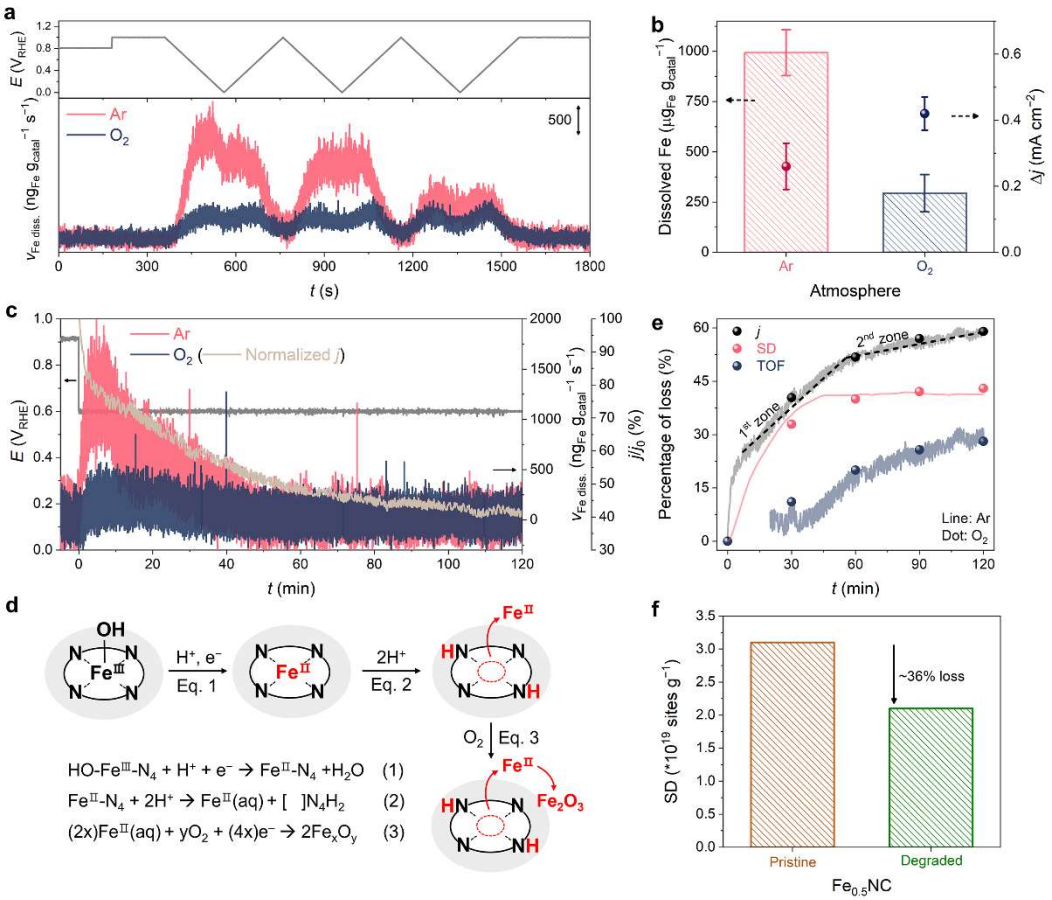

Fig. 2. Effects of Ar and O_2 gases on Fe dissolution of $Fe_{0.5}NC$. a, Real-time Fe dissolution of $Fe_{0.5}NC$/GDE obtained by *online* GDE/EFC/ICP-MS during the three CVs in a potential range of 1.0–0.0 V_{RHE} under Ar or O_2 flow at 353 K. The electrolyte was de-aerated 0.1 M $HClO_4$. **b**, Cumulative amounts of dissolved Fe and ORR activity loss obtained after the three CVs under Ar or O_2 flow. The activity loss was recorded at 0.8 V_{RHE} after the CVs (Supplementary Figs. 13 and 14). Error bars (SD) are calculated based on three independent experiments. **c**, Real-time Fe dissolution of $Fe_{0.5}NC$/GDE obtained by *online* GDE/EFC/ICP-MS during the potential hold at 0.6 V_{RHE} under Ar or O_2 flow at 353 K for 2 h. The electrolyte was de-aerated 0.1 M $HClO_4$. The relative change in ORR current density is also shown. **d**, A proposed mechanism for Fe demetallation from $Fe_{0.5}NC$. **e**, Relative loss of *j*, SD, and TOF values as a function of operation time obtained during the potential hold at 0.6 V_{RHE} and 353 K under O_2 (dot) or Ar flow (line). SD loss under O_2 flow was derived from the sum of cumulative Fe-N_4 dissolution (measured by GDE/EFC/ICP-MS) and Fe oxides amounts (measured by post-leaching), whereas that under Ar flow was directly derived from the cumulative Fe-N_4 dissolution only owing to lack of the Fe oxides formation (Supplementary Fig. 25). **f**, SD value of pristine or degraded $Fe_{0.5}NC$ measured by nitrite stripping assuming a three-electron transferred reduction of nitrosyl ligand or NO (*i.e.*, NO to NH_2OH).[21]

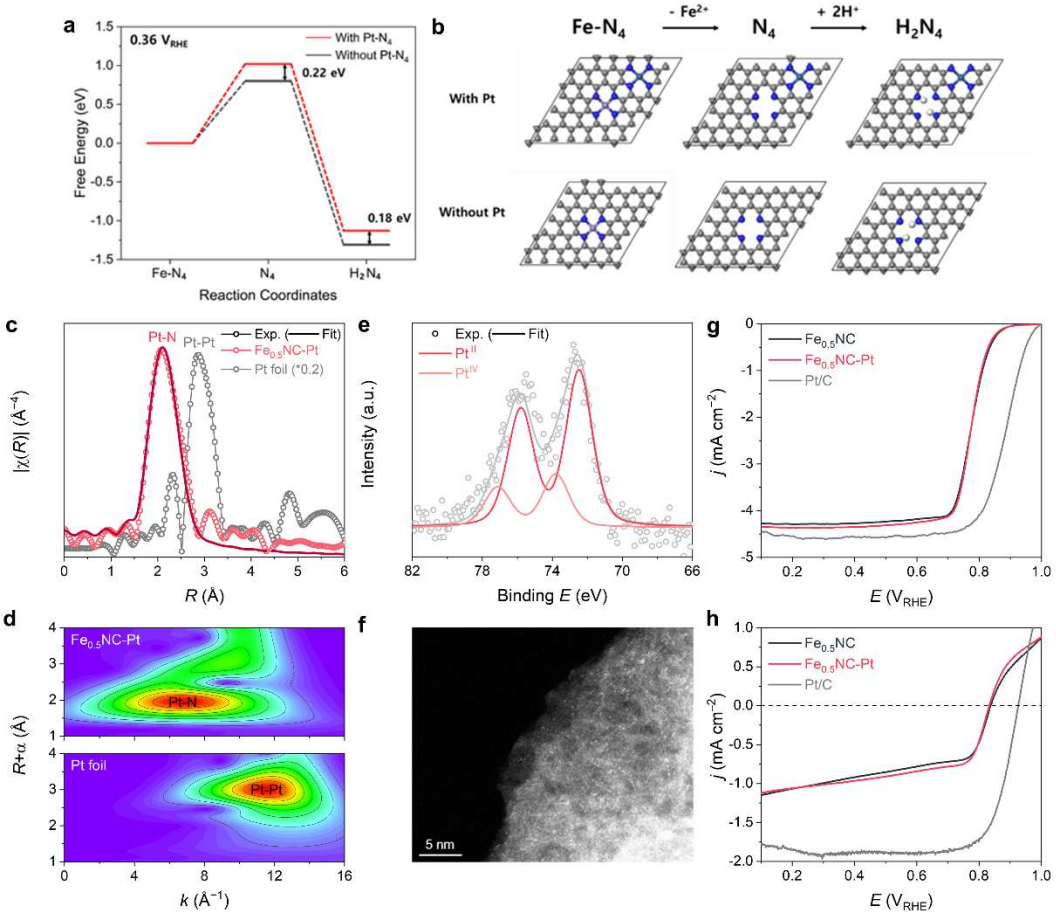

Fig. 3. Physical and electrochemical characterizations of $Fe_{0.5}$NC-Pt. a,b, DFT reaction free energy profiles of the Fe dissolution process (Eq. 2 in Fig. 2d) of Fe-N_4 system with/without Pt-N_4 site (**a**), and corresponding DFT-optimized structures (**b**). With the Pt-N_4 site, DFT energetics predict less favorable energetics of the Fe dissolution. White, gray, blue, purple, and green represent the H, C, N, Fe, and Pt atoms, respectively. **c,d**, k^3-weighted Pt L_3-edge FT-EXAFS (**c**) and WT-EXAFS (**d**) spectra of $Fe_{0.5}$NC-Pt and Pt foil. **e**, XPS-Pt_{4f} spectrum. **f**, HAADF-STEM image of $Fe_{0.5}$NC-Pt (scale bar = 5 nm). **g**,**h**, ORR (**g**) and PRR (**h**) polarization curves of $Fe_{0.5}$NC-Pt measured with RDE in a 0.1 M $HClO_4$ electrolyte at 900 rpm. For comparison, those for $Fe_{0.5}$NC or Pt/C are also shown.

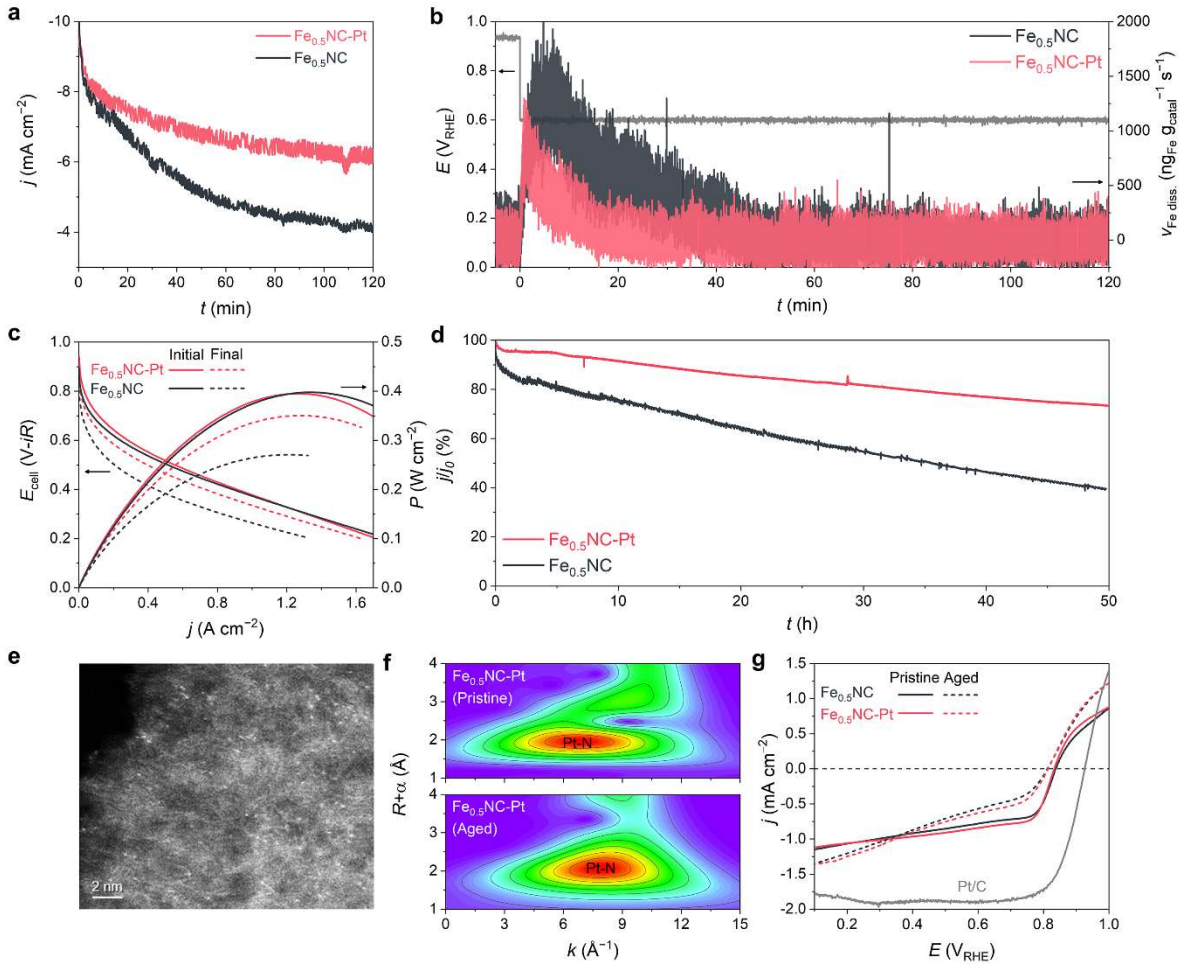

Fig. 4. Proof-of-concept strategy with isolated Pt ion as a stabilizer of Fe-N$_4$ sites. a,**b**, ORR current density (**a**) and real-time Fe dissolution under Ar flow (**b**) of $Fe_{0.5}$NC/GDE and $Fe_{0.5}$NC-Pt/GDE obtained by *online* GDE/EFC/ICP-MS during 2 h potential hold at 0.6 V_{RHE} and 353 K. The electrolyte was de-aerated 0.1 M $HClO_4$. **c**, *iR*-corrected H_2/O_2 fuel cell polarization curves and corresponding power density curves before and after 50 h operation at 0.5 V. **d**, Normalized current density *vs.* time obtained during 50 h operation at 0.5 V. **e**, HAADF-STEM image of $Fe_{0.5}$NC-Pt obtained after 50 h operation at 0.5 V (scale bar = 2 nm). **f,** k^3-weighted Pt L_3-edge WT-EXFAS plots of $Fe_{0.5}$NC-Pt before and after 50 h operation at 0.5 V. **g**, PRR polarization curves of $Fe_{0.5}$NC and $Fe_{0.5}$NC-Pt before and after 50 h operation at 0.5 V measured with RDE in an Ar-saturated 0.1 M $HClO_4$ electrolyte at 900 rpm. For comparison, the initial PRR polarization curve of Pt/C is also shown.